

Quantum Dots embedded in Graphene Nanoribbons by Chemical Substitution

Eduard Carbonell-Sanromà,[†] Pedro Brandimarte,^{‡,¶} Richard Balog,^{†,§,||} Martina
Corso,^{†,‡,§} Shigeki Kawai,^{⊥,#,@} Aran Garcia-Lekue,^{¶,§} Shohei Saito,^{@,△} Shigehiro
Yamaguchi,[▽] Ernst Meyer,[#] Daniel Sánchez-Portal,^{‡,¶} and Jose Ignacio
Pascual^{*,†,§}

[†]*CIC nanoGUNE, Tolosa Hiribidea 76, 20018 Donostia-San Sebastian, Spain*

[‡]*Centro de Fisica de Materiales, 20018 Donostia-San Sebastian, Spain*

[¶]*Donostia International Physics Center, 20018 Donostia-San Sebastian, Spain*

[§]*Ikerbasque, Basque Foundation for Science, Bilbao, Spain*

^{||}*Department of Physics and Astronomy, Aarhus University, Ny Munkegade 120, Bld.
1520, 8000 Aarhus C, Denmark*

[⊥]*99 International Center for Materials Nanoarchitectonics, National Institute for
Materials Science, 1-1, Namiki, Tsukuba, Ibaraki 305-0044, Japan*

[#]*Department of Physics, University of Basel, CH-4056 Basel, Switzerland*

[@]*PRESTO, Japan Science and Technology Agency, Kawaguchi, Saitama 332-0012, Japan*

[△]*999 Department of Chemistry, Graduate School of Science, Kyoto University,
Kitashirakawa Oiwake, Sakyo, Kyoto 606-8502, Japan*

[▽]*Institute of Transformative Bio-molecules, Nagoya University, Furo, Chikusa, Nagoya
464-8602, Japan*

E-mail: ji.pascual@nanogune.eu

Abstract

Bottom-up chemical reactions of selected molecular precursors on a gold surface can produce high quality graphene nanoribbons (GNR). Here, we report on the formation of quantum-dots embedded in an armchair GNR by substitutional inclusion of pairs of boron atoms into the GNR backbone. The boron inclusion is achieved through the addition of a small amount of boron substituted precursors during the formation of pristine GNR. In the pristine region between two boron pairs, the nanoribbons show a discretization of their valence band into confined modes compatible with a Fabry-Perot resonator. Transport simulations of the scattering properties of the boron pairs reveal that they selectively confine the first valence band of the pristine ribbon while allowing an efficient electron transmission of the second one. Such band-dependent electron scattering stems from the symmetry matching between the electronic wave functions of the states from the pristine nanoribbons and those localized at the boron pairs.

Keywords

Scanning Tunneling Microscopy, Scanning Tunneling Spectroscopy, Graphene Nanoribbon, Quantum Dot, On-surface Synthesis, Electronic Transport

One-dimensional conjugated systems are ideal materials for organic optoelectronics because they combine large intrinsic charge carrier mobility with low defect density and higher structural order. However, the interface of these systems with active elements and junctions is usually more disordered than in epitaxial grown inorganic interfaces. A promising strategy is the use of graphene nanoribbons (GNRs) because they combine the large electron mobility from graphene with an energy band gap that depends on their width and shape.^{1,2} This enables the creation of optically active heterostructures in the carbon system itself. Defect-free GNRs can be bottom-up assembled by on-surface reactions of molecular organic precursors over a metal surface. This technique can produce ribbons with armchair³ or zigzag⁴ edges, intermediate chiral alignments,⁵ as well as tune the ribbon's bandgap by proper selection of the shape of the organic precursor.⁶⁻⁸ In this way, GNR heterostructures have been constructed by combining precursors of different width or with substitutional heteroatoms.^{9,10}

The versatility of this on-surface chemical toolbox paves the way for the atomically precise growth of hybrid GNRs with active elements for becoming operational nanodevices. One of such elements are quantum dots (QDs). QDs embedded inside a GNR may turn it optically active for luminescence when electrically powered through the terminal GNR segments. The construction of such hybrid devices requires a precise technology to create confining barriers for electrons inside the nanoribbon.^{9,11}

Here, we show that the insertion of a pair of substitutional heteroatoms in the interior of the ribbon backbone produces very efficient confining barriers for electrons, leading to quantum well (QW) states in their valence band (VB). We produce these hybrid AGNRs by adding a small amount of boron-substituted precursors during the on-surface reaction of DBBA molecules (Figure 1a) to produce 7-AGNRs following the method reported by Cai *et al.*³ The borolated precursor, here labeled 2B-DBBA,^{12,13} has a 9,10-dihydro-9,10-diboraanthracene moiety in the middle of the DBBA molecule (Figure 1b). In this way, it inserts two substitutional boron atoms inside the carbon backbone, while preserving the overall shape and width of the created 7-AGNR. The mixture of DBBA and 2B-DBBA

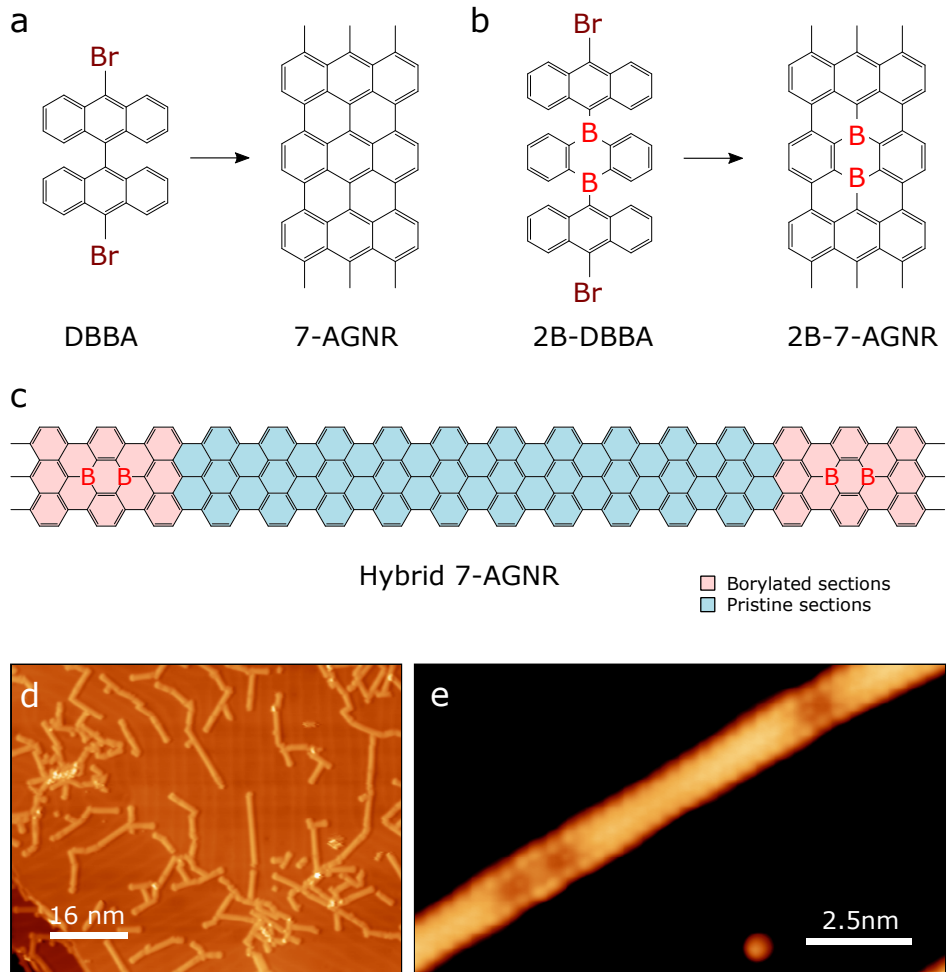


Figure 1: (a) Molecular structure of 10,10'-dibromo-9,9'-bianthryl (DBBA) precursors and the resulting 7-AGNR. (b) Structure of the precursor 9,10-bis(10-bromoanthracen-9-yl)-9,10-dihydro-9,10-diboraanthracene (2B-DBBA) and the resulting boron substituted 2B-7-AGNR.^{12,13} (c) Chemical structure of a hybrid 7-AGNR formed after on-surface reaction of five DBBA precursors between two 2B-DBBA molecules. Pink (blue) sections mark the borylated (pristine) regions on the hybrid structure. (d) Overview STM image of a Au(111) surface precovered with hybrid 7-AGNRs ($V_s=0.6$ V, $I=70$ pA). (e) Small-scale STM image of a hybrid 7-AGNR ($V_s=1$ V, $I=1.7$ nA). The dark spots at the center of the ribbon allows us to identify the position of the boron pairs.

precursors thus results in ribbons with a pristine 7-AGNR body and a few subunits of substitutional boron pairs (Fig. 1c). The boron pairs locally modify the electronic properties of the 7-AGNR segments.¹² Using Scanning Tunneling Spectroscopy (STS), we find that the valence band of pristine segments between two 2B sites is discretized into states with an integer number of modes, resembling a Fabry-Perot resonator for GNR electrons.^{14,15}

Electronic transport calculations reveal that the borylated segments act as perfect scatterers for VB electrons, but are transparent for the band below (VB-1). We show that this band-selective scattering depends on the difference in wave-function symmetry between 7-AGNRs bands and localized states at boron pairs. The band-specific scattering of electrons suggests that active components such as QDs can be embedded in GNRs, while maintaining fully transmitting channels for hole injection.

As observed from the STM images (Figure 1d), DBBA and 2B-DBBA precursors aggregate to produce linear hybrid 7-AGNR of homogeneous width. At a sample bias $V_s=1$ V (Figure 1e) the borylated subunits appear as a characteristic depression in the center of the GNR backbone.¹³ A mixture ratio $\sim 3:1$ of DBBA and 2B-DBBA precursors leads to ribbons that consist of a pristine GNR body with randomly distributed pairs of boron atoms along the ribbon, with an average distance of more than 3 nm.

To determine the effect of embedded boron-pairs on the electronic structure of the ribbon we performed STS measurements at different positions. The spectrum on the edge of the pristine segments shows valence and conduction bands with onsets at -0.8 eV and 1.7 eV, respectively (Figure 2a, blue), giving an transport band gap of 2.5 eV, in agreement with Refs.^{16,17} At the edges of the 2B sites, the VB of the pristine regions is completely absent (Fig. 2a, red), while the conduction band (CB) appears unaffected by the presence of boron substituents. The absence of VB signal at the borylated segments is clearly observed in differential conductance (dI/dV) maps measured at $V_s=-0.8$ V, i.e. at the pristine VB onset (Figure 2c). An enhanced dI/dV signal is mostly observed along the ribbon edges of pristine parts,^{9,16} appearing strongly suppressed around the boron sites. The dI/dV maps additionally reveal that boron pairs exhibit two localized states at -2 eV and -0.6 eV (Figs. 2b and 2d, respectively).

The VB suppression indicates that the 2B sites act as scattering centers for electrons. Indeed, the valence band of pristine nanoribbon sections enclosed by two borylated subunits shows fingerprints of energy discretization (Fig. 3a) suggesting quantum confinement of

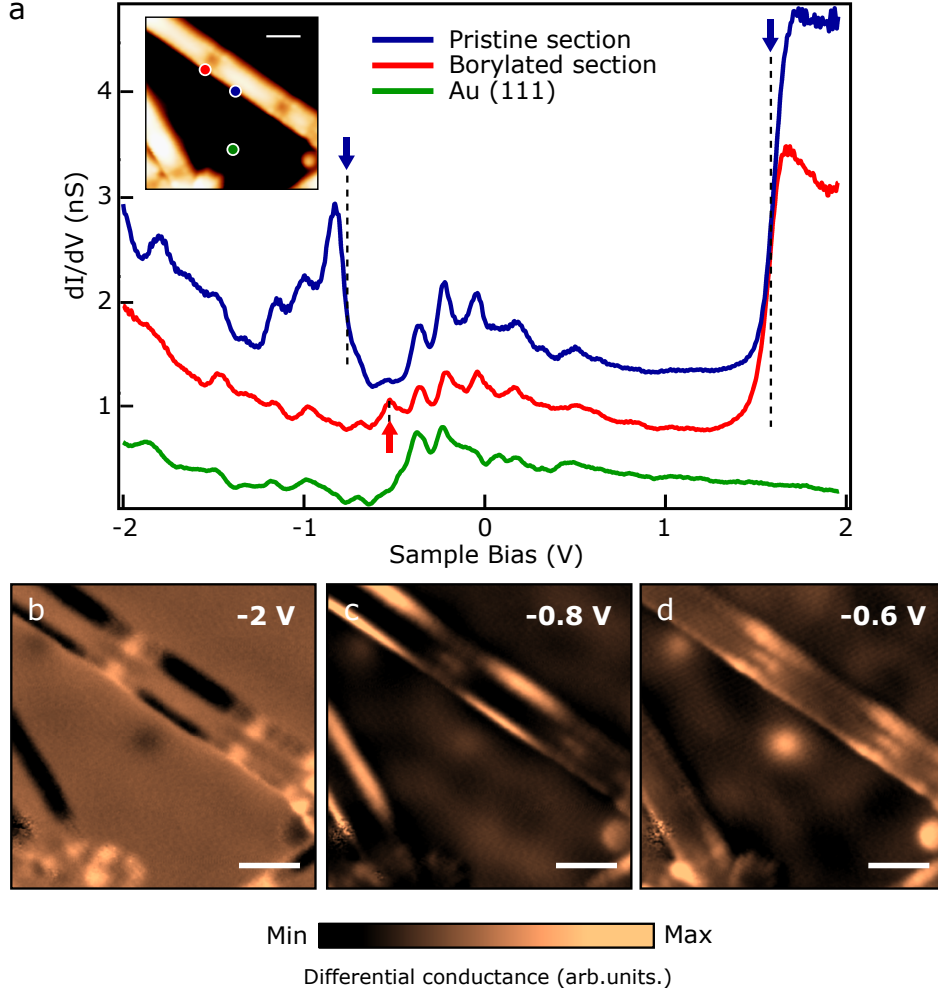


Figure 2: (a) Differential conductance (dI/dV) spectra taken at different sites of the hybrid GNR. Blue spectrum acquired at the edge of a pristine section. Red spectrum acquired at the edge of a boronated section. Green spectrum acquired over the Au(111) substrate. Blue arrows and dashed lines mark the onset of the CB for the pristine and boronated section and the onset of the VB for the pristine segment. Red arrow marks the boron localized state in Fig 2d. All spectra were taken with the same tip and are vertically offset for clarity (open-feedback parameters: $V_s=1.0$ V, $I=0.41$ nA, $V_{rms}=12$ mV, $f=767.7$ Hz). States between -0.45 eV and 0.5 eV are the Shockley surface state band of Au(111). The peaks below the VB onset, at -0.9 V and -1.1 V, are due to band discretization, discussed later in the main text. (b) Constant current differential conductance maps of the hybrid nanoribbon shown in the inset of Figure 2a at $V_s=-2$ V, showing a localized state around the boron regions. (c) Same as in b but bias voltage is chosen at the energy of the onset of the pristine VB, $V_s=-0.8$ V. (d) Same as in b but at a bias voltage where the first localized states of the boronated sections appear, $V_s=-0.6$ V. Differential conductance maps feedback conditions: $I=0.5$ nA, $V_{rms}=16$ mV, $f=767.7$ Hz. All scale bars are 1.8 nm.

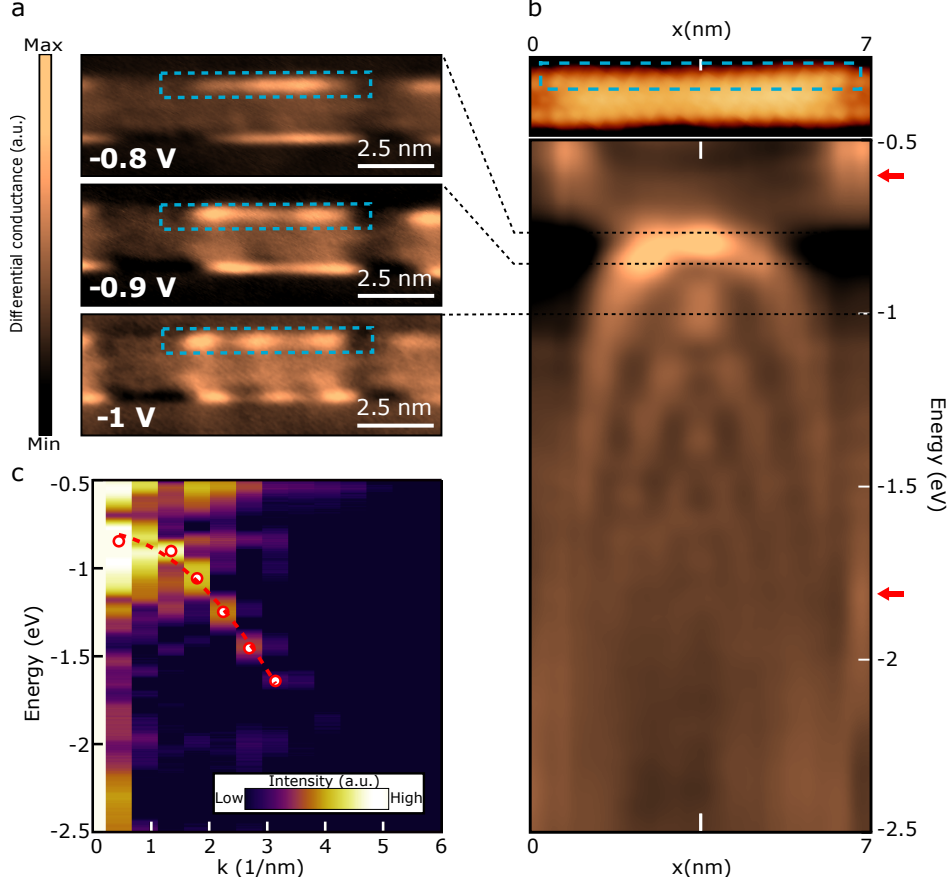


Figure 3: (a) Constant current differential conductance maps of hybrid GNR, taken at energies where the spatial modulation of the VB of the pristine sections is seen. The maps show from one up to three maxima. Dark regions at the edge of the ribbon coincide with the position of the borolated sections of the ribbon. Differential conductance maps feedback conditions: $I=0.5$ nA, $V_{rms} = 20$ mV, $f = 743.4$ Hz. (b) Stack plot of constant current differential spectra taken along the edge (marked in the topography image on top with blue dotted rectangle) of a pristine section confined between two borolated sections. Red arrows mark the 2B localized states of figure 2b and 2d. Constant current feedback conditions: $I=1$ nA, $V_{rms} = 14$ mV, $f = 743.4$ Hz (c) Line-by-line Fourier Transform of b, including the parabolic fit used for extracting $E(k=0)$ and m^* .

electrons. dI/dV maps show that the valence band appears with a series of maxima along the edges of the nanoribbon. Furthermore, the number of maxima increases with bias voltage, which is characteristic of a quantum well (QW) system.

A dI/dV spectral map along the pristine GNR segment depicts the full energy distribution of the VB quantum well states (Figure 3b). The first QW state is located at -0.85 eV, and overlaps with the second one due to their energy broadening. The third state located at

-1 eV has three evident maxima. The quantized levels go as high as $N=7$ at an energy of -1.7 eV. Below this energy, no additional confined states are observed, probably due to their overlap with the state localized at the 2B sites at -2 eV (Figure 2b).

The line-by-line Fast Fourier Transform (FFT) of Figure 3b reproduces the dispersive behavior of the confined VB (Figure 3c). From a parabolic fit $E(k) = E(k=0) + \hbar^2 k^2 / 2m^*$ of the FFT-STs spectral map we deduce a band effective mass of $m^* = 0.43 \pm 0.03m_e$, in correspondence with pristine 7-AGNRs.^{16,18} Additionally we estimate from the fit that the top of the band lies at $E(k=0) = -0.79 \pm 0.03$ eV as in bare 7-AGNR.¹⁶ Therefore, we conclude that boron pairs do not act as charge dopants, but only as scatterers.

In order to investigate the origin of the band confinement we performed first principles calculations via Density Functional Theory (DFT) on a free-standing 7-AGNR with two diboron substituted subunits separated ~ 65 Å apart which behave as charge acceptors (see Methods and Fig. S1 in Supporting Information¹⁹). The open system was simulated by coupling each terminal from the hybrid GNR to semi-infinite pristine ribbons, which act as electrodes. We first calculated the density of states (DOS) along the central pristine segment, and project it onto atomic columns across the 7-AGNR section.²⁰ Figure 4a depicts the corresponding projected DOS (PDOS) plotted along the confined region, showing that it consists of discrete levels with an integer number of DOS maxima between the boron subunits, as in the experimental dI/dV spectral map of Fig. 3b. From the evolution of the confined levels with energy we obtain an effective mass of $m^* = 0.36 \pm 0.02m_e$ (see methods). The small difference of band's effective mass with respect to the experiment might be related to the role of the surface, not included in the simulations.

The DFT results thus confirm the strong confinement of the valence band between boron pair sites, suggesting that they behave as very effective scatterers for VB electrons. To get more insight on the scattering properties of these sites we simulated the electronic transport through these hybrid graphene nanoribbons (see methods). Figure 4b compares the energy-dependent electronic transmission (probability of an electron to propagate from one electrode

to the other) along a pristine ribbon (red) with the case of including a single boron pair site (green-dashed) and two of them forming a quantum well (blue). The transmission through a pristine 7-AGNR shows a typical step-like behavior with the opening of new channels corresponding to the available bands (VB and VB-1 in the plotted energy window). The effect of including a single 2B site in the ribbon is drastic: the transmission of the VB is almost completely suppressed. In contrast, the VB-1 is apparently not affected by the impurity, exhibiting an onset to a baseline of transmission about 1. Thus, a single boron pair acts as a hard barrier for VB electrons but is fully transparent for VB-1 electrons.

This peculiar band selective behavior is also expressed in the transmission through the double 2B quantum-well case. The VB shows zero transmission except for narrow peaks of $T \sim 1$ at the energy of the QW states, supporting that this system is the electron analog of a Fabry-Perot (FP) resonator. At the onset of the VB-1 (laying at -0.87 eV see Fig. S2 in Supporting Information¹⁹), the transmission shows again a step like behavior to $T \sim 1$, and resonant peaks reaching $T \sim 2$. Looking at the eigenchannel’s wavefunctions (see Methods) at energies between resonant peaks (Fig. 4c), we resolve that the baseline $T \sim 1$ corresponds to the VB-1, which is fully transmitted through the double-barrier system. The VB is strongly reflected at the first 2B-site, except for the energy of the QW states, where it expands with the node structure in the resonator (Fig. 4d) and transmits with narrow FP-peaks. The FP resonator is manifested not only in the node structure, but also in a higher wavefunction amplitude between the 2B-sites when compared to the incoming wave. From the sharp transmission lines at the Fabry-Perot modes we corroborate that 2B sites reflect VB electrons with $R \sim 1$. We note that this is in absence of any surface acting as support. In the experiments, the linewidth of the quantum levels is significantly broader due to the presence of a metal surface.

The origin of the band selectivity in the electron scattering is related to the specific symmetry of the electronic wave functions of AGNR bands and boron-induced states. Figure 4e shows the Highest Occupied Molecular Orbital of a molecule simulating the borylated 7-

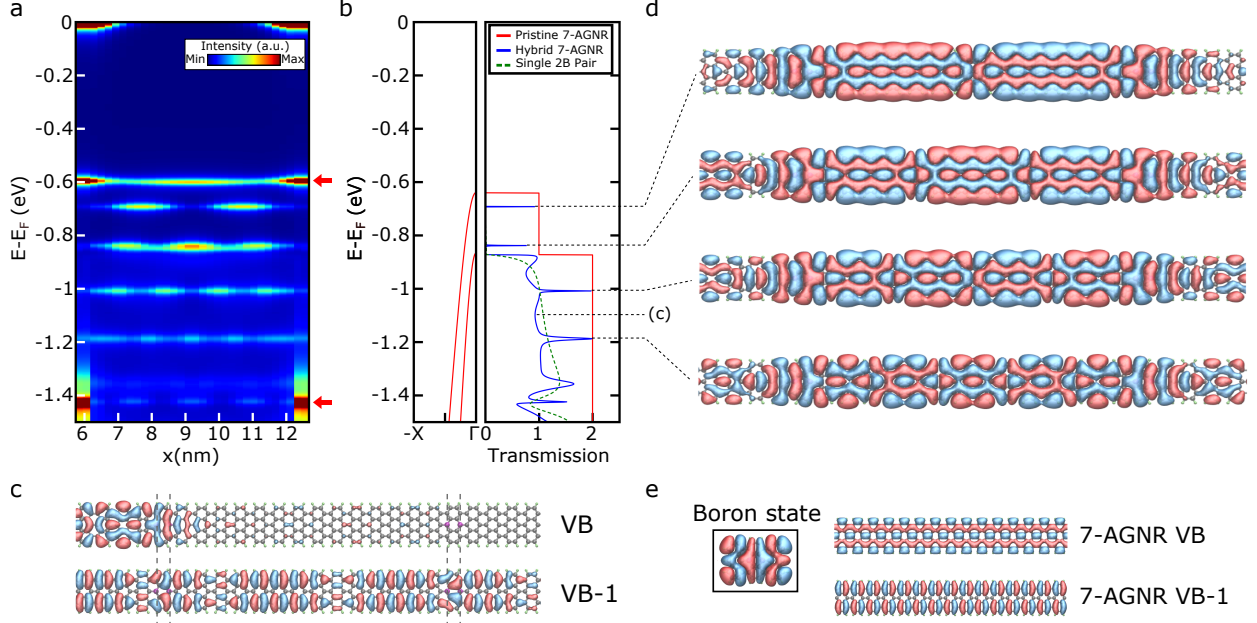


Figure 4: (a) PDOS for a pristine segment enclosed between two borylated sections 65 Å apart. Quantized levels up to $N=5$ are clearly observed between the boron localized states. Red arrows show boron resonances with strong boron p_z character, corresponding to localized states found in the spectral map of Fig. 3b. (b) VB and VB-1 dispersion for a pristine 7-AGNR (left) and Transmission function (right) for a pristine ribbon (red), a single boron pair (dashed green) and for the confined system formed by two boron pairs (blue). The transmission function shows the strong reflectivity of a single boron pair and the Fabry-Perot behavior of the double 2B-barrier system. The transmission through the $N=1$ quantum level is not seen because this state lies in the energy gap of the electrodes (Fig. S5 in Supporting Information¹⁹) (c) Real part of the eigenchannel functions taken at $E - E_F = -1.10$ eV (dashed-dot line in panel 4b), i.e. between quantized levels. The eigenchannel corresponding to the VB shows no transmission through the boron segments, while VB-1 fully transmits through. (d) Real part of the eigenchannel functions taken at the energies corresponding to the $N=2,3,4$ and 5 quantum well levels. (e) Real part of the wavefunctions for the boron-induced state (calculated for a borylated monomer, see Fig. S3 in Supporting Information¹⁹), and for the pristine 7-AGNR VB and VB-1 bands at Γ -point. Both the boron state and the VB show an even symmetry with respect to the mirror plane bisecting the GNR along its axis, while VB-1 has odd symmetry.

AGNR segment (see Fig. S3 in Supporting Information¹⁹), which has the strongest boron p_z character. This state reflects the symmetry of the boron localized states in the hybrid 7-AGNR, marked in Figure 4a with red arrows (Fig. S4 in Supporting Information¹⁹). In particular, this state has an even symmetry across the AGNR.²¹ VB states are also even-symmetric across the AGNR, while VB-1 states have odd symmetry and, hence, expose a

nodal plane at the center of the AGNR backbone (Fig. 4e). Therefore, boron-localized states hybridize with the valence band,²² but are orthogonal to the VB-1 band. The boron states also present a nodal plane at the center of the boron pair, which imposes a phase change of π in the constant-phase propagation of VB states along the AGNR growth direction. This is the origin of the large VB-scattering at the 2B-sites. The VB-1 transmits freely because it cannot mix with boron states, and its wavefunction amplitude remains essentially unaffected by the 2B-segments. In the experiments, the VB-1 onset is weakly sampled by the STM tip [16] and, therefore, hardly visible in point dI/dV spectra. This band, if confined, should be easier to detect due to its localized character. Additional modes should arise around -1.5 eV,^{17,23} which is not the case in our experiments, supporting the absence of VB-1 confinement.

In conclusion, we have shown that hybrid 7-AGNRs with a small amount of 2B substitutional subunits give rise to quantum-well states due to electron confinement in the region between two 2B sites. The boron pair units act as local scatterers for one of the two valence bands of the 7-AGNR while leaving the other unaffected. First principles calculations on a free standing hybrid 7-AGNR qualitatively reproduce our experimental results and evidence that the band selective nature of the confinement is due to the different symmetry of the bands of the pristine ribbon and the scatterer states; only states with matching symmetry are affected. The presented band-selective procedure to manipulate only some bands envisions embedding functional devices in GNRs while transmitting charge through other unaffected bands. Furthermore, our results indicate that the substitutional doping of conjugated conductors with heteroatoms goes beyond a simple charge doping model and can be a method to manipulate bands' wave-function and transport channels.

Methods

Our experiments were performed in custom designed low temperature STM, under ultra-high vacuum, and at 4.2 K. An atomically clean Au(111) single crystal surface was precovered with a mixture of DBBA and 2B-DBBA molecular precursors via sequential thermal sublimation from two knudsen cells at 180°C and 290°C, respectively. A 3:1 ratio between the molecules was used to ensure a majority of pristine 7-AGNR segments. Subsequently, the step-growth polymerization of the precursors was induced by annealing the sample at 200°C. Finally, annealing the sample to 400°C lead to a cyclodehydrogenation step required for the formation of 7-AGNRs, as reported on previous works.³ We measured the differential conductance by applying a small modulation to the sample bias and using the lockin technique to obtain a signal proportional to dI/dV from the first harmonic of the tunneling current. The spectral map of Fig. 3b was obtained in close feedback-loop mode, which allowed scanning a large energy window by correcting the tunneling transmission with the tip-sample distance. This method improves the resolution of spectroscopic features over a continuous background and provides a closer agreement of point $dI/dV(V)$ spectra with $DOS(E)$. The topography contours in the bias range of the quantum-well features didn't show any modulation along the lenght of the ribbon, thus discarding their influence in the results.^{24,25} A total of three energy dispersion relations were extracted for quantum wells of different lengths (see Figure S6 in Supporting information¹⁹). First principles calculations were carried out for a free-standing 7-AGNR with two B-substituted subunits at a distance of ~ 65 Å. Our electronic structure calculations were performed using the SIESTA/TranSIESTA package,^{26,27} that allow performing open boundary calculations. We use the van der Waals density functional by Dion *et al*²⁸ with exchange modified by J. Klimeš, D. Bowler and A. Michaelides.²⁹ The core electrons were described by nonlocal Troullier-Martins pseudopotentials³⁰ and we used a double- ζ basis set to expand the valence-electron wavefunctions. The real-space grid was defined using a 250 Ry energy cutoff. The structure was allowed to fully relax using conjugate gradient method with a force tolerance of $10 \text{ meV}\text{\AA}^{-1}$. A value of $m^*=0.36$ me for the

effective mass of the confined segment was obtained by fitting the modes and their energies to a particle in a box model with hard walls. For a pristine 7-AGNR our theory obtain a parabolic dispersion with $m^*=0.33 m_e$ for states close to Gamma point. The eigenchannel wave functions, which in the electrodes are given by linear combination of scattering states such that diagonalize the transmission matrix at a given energy, were calculated with the Inelastica code.^{31,32} While the electrostatics of standard SIESTA calculations assume 3D boundary conditions, in order to avoid artifacts in our treatment of the electrostatic interactions we use a cylindrical cutoff for the Coulomb interaction (i.e., Coulomb interaction is finite range in the directions perpendicular to ribbon axis), with a cutoff radius of 12.5 Å, so the system is treated as strictly 1-D from the point of view of electrostatics.³³

Acknowledgements

The authors thank D.G. de Oteyza for his insights in effective mass calculations and T. Frederiksen for invaluable discussions and guidance in eigenchannel wave functions calculations. This work was supported by FP7 FET-ICT “Planar Atomic and Molecular Scale devices” (PAMS) project (funded by the European Commission under contract No. 610446), by the Spanish Ministerio de Economía y Competitividad (MINECO) (Grants No. MAT2013-46593-C6) and the Basque Government (Dep. de Educación and UPV/EHU, Grant No. IT-756-13, and Dep. Industry, Grant PI_2015_1_42), by the Japan Science and Technology Agency (JST) “Precursory Research for Embryonic Science and Technology (PRESTO)” for a project of “Molecular technology and creation of new function”, and by JSPS KAKENHI Grant Number 15K21765.

References

- (1) Nakada, K.; Fujita, M.; Dresselhaus, G.; Dresselhaus, M. S. Edge state in graphene ribbons: Nanometer size effect and edge shape dependence. *Phys. Rev. B* **1996**, *54*,

17954–17961.

- (2) Son, Y.-W.; Cohen, M. L.; Louie, S. G. Energy Gaps in Graphene Nanoribbons. *Physical Review Letters* **2006**, *97*, 216803.
- (3) Cai, J.; Ruffieux, P.; Jaafar, R.; Bieri, M.; Braun, T.; Blankenburg, S.; Muoth, M.; Seitsonen, A. P.; Saleh, M.; Feng, X.; Müllen, K.; Fasel, R. Atomically precise bottom-up fabrication of graphene nanoribbons. *Nature* **2010**, *466*, 470–473.
- (4) Ruffieux, P.; Wang, S.; Yang, B.; Sánchez-Sánchez, C.; Liu, J.; Dienel, T.; Talirz, L.; Shinde, P.; Pignedoli, C. A.; Passerone, D.; Dumslaff, T.; Feng, X.; Müllen, K.; Fasel, R. On-surface synthesis of graphene nanoribbons with zigzag edge topology. *Nature* **2016**, *531*, 489–492.
- (5) de Oteyza, D. G.; García-Lekue, A.; Vilas-Varela, M.; Merino-Díez, N.; Carbonell-Sanromà, E.; Corso, M.; Vasseur, G.; Rogero, C.; Guitián, E.; Pascual, J. I.; Ortega, J. E.; Wakayama, Y.; Peña, D. Substrate-Independent Growth of Atomically Precise Chiral Graphene Nanoribbons. *ACS Nano* **2016**, *10*, 9000–9008.
- (6) Chen, Y.-C.; de Oteyza, D. G.; Pedramrazi, Z.; Chen, C.; Fischer, F. R.; Crommie, M. F. Tuning the Band Gap of Graphene Nanoribbons Synthesized from Molecular Precursors. *ACS Nano* **2013**, *7*, 6123–6128.
- (7) Basagni, A.; Sedona, F.; Pignedoli, C. A.; Cattelan, M.; Nicolas, L.; Casarin, M.; Sambri, M. Molecules-Oligomers-Nanowires-Graphene Nanoribbons: A Bottom-Up Stepwise On-Surface Covalent Synthesis Preserving Long-Range Order. *J. Am. Chem. Soc.* **2015**, *137*, 1802–1808.
- (8) Kimouche, A.; Ervasti, M. M.; Drost, R.; Halonen, S.; Harju, A.; Joensuu, P. M.; Sainio, J.; Liljeroth, P. Ultra-narrow metallic armchair graphene nanoribbons. *Nature Communications* **2015**, *6*, 10177.

- (9) Chen, Y.-C.; Cao, T.; Chen, C.; Pedramrazi, Z.; Haberer, D.; de Oteyza, D. G.; Fischer, F. R.; Louie, S. G.; Crommie, M. F. Molecular bandgap engineering of bottom-up synthesized graphene nanoribbon heterojunctions. *Nature Nanotechnology* **2015**, *10*, 156–160.
- (10) Cai, J.; Pignedoli, C. A.; Talirz, L.; Ruffieux, P.; Söde, H.; Liang, L.; Meunier, V.; Berger, R.; Li, R.; Feng, X.; Müllen, K.; Fasel, R. Graphene nanoribbon heterojunctions. *Nature Nanotechnology* **2014**, *9*, 896–900.
- (11) Biel, B.; Blase, X.; Triozon, F.; Roche, S. Anomalous Doping Effects on Charge Transport in Graphene Nanoribbons. *Physical Review Letters* **2009**, *102*, 096803.
- (12) Cloke, R. R.; Marangoni, T.; Nguyen, G. D.; Joshi, T.; Rizzo, D. J.; Bronner, C.; Cao, T.; Louie, S. G.; Crommie, M. F.; Fischer, F. R. Site-Specific Substitutional Boron Doping of Semiconducting Armchair Graphene Nanoribbons. *Journal of the American Chemical Society* **2015**, *137*, 8872–8875.
- (13) Kawai, S.; Saito, S.; Osumi, S.; Yamaguchi, S.; Foster, A. S.; Spijker, P.; Meyer, E. Atomically controlled substitutional boron-doping of graphene nanoribbons. *Nature Communications* **2015**, *6*, 8098.
- (14) Bürgi, L.; Jeandupeux, O.; Hirstein, A.; Brune, H.; Kern, K. Confinement of surface state electrons in Fabry-Pérot resonators. *Physical Review Letters* **1998**, *81*, 5370.
- (15) Schirone, S.; Krasovskii, E.; Bihlmayer, G.; Piquerel, R.; Gambardella, P.; Mugarza, A. Spin-Flip and Element-Sensitive Electron Scattering in the BiAg₂ Surface Alloy. *Physical Review Letters* **2015**, *114*, 166801.
- (16) Söde, H.; Talirz, L.; Gröning, O.; Pignedoli, C. A.; Berger, R.; Feng, X.; Müllen, K.; Fasel, R.; Ruffieux, P. Electronic band dispersion of graphene nanoribbons via Fourier-transformed scanning tunneling spectroscopy. *Physical Review B* **2015**, *91*, 045429.

- (17) Ruffieux, P.; Cai, J.; Plumb, N. C.; Patthey, L.; Prezzi, D.; Ferretti, A.; Molinari, E.; Feng, X.; Müllen, K.; Pignedoli, C. A.; Fasel, R. Electronic Structure of Atomically Precise Graphene Nanoribbons. *ACS Nano* **2012**, *6*, 6930–6935.
- (18) Wang, S.; Talirz, L.; Pignedoli, C. A.; Feng, X.; Müllen, K.; Fasel, R.; Ruffieux, P. Giant edge state splitting at atomically precise graphene zigzag edges. *Nature Communications* **2016**, *7*, 11507.
- (19) See online Supporting Information.
- (20) In the PDOS an artificial broadening of 10 meV was used on the electrodes and scattering region, for a better visualization. All other calculations were performed with a broadening of 10^{-6} eV.
- (21) VB has an even mirror symmetry regarding the plane defined by the AGNR growing direction and a vector normal to the ribbon plane.
- (22) This hybridization has been also verified by investigating the wave functions obtained from a periodic calculation of a 7-AGNR with a single boron dimer (see Fig. S4 in Supporting Information).
- (23) Experimentally, Ruffieux *et al.*¹⁷ reports this band onset to lay approximately 0.7 eV below the VB using photoemission spectroscopy on a vicinal Au surface. Extrapolating this results to the Au(111) surface, we would expect to find this band starting at -1.5 eV.
- (24) Li, J.; Schneider, W.-D.; Berndt, R. Local density of states from spectroscopic scanning-tunneling-microscope images: Ag (111). *Physical Review B* **1997**, *56*, 7656.
- (25) Krenner, W.; Kühne, D.; Klappenberger, F.; Barth, J. V. Assessment of Scanning Tunneling Spectroscopy Modes Inspecting Electron Confinement in Surface-Confined Supramolecular Networks. *Scientific Reports* **2013**, *3*, 1454.

- (26) Soler, J. M.; Artacho, E.; Gale, J. D.; García, A.; Junquera, J.; Ordejón, P.; Sánchez-Portal, D. The SIESTA method for ab initio order- N materials simulation. *Journal of Physics: Condensed Matter* **2002**, *14*, 2745.
- (27) Brandbyge, M.; Mozos, J.-L.; Ordejón, P.; Taylor, J.; Stokbro, K. Density-functional method for nonequilibrium electron transport. *Physical Review B* **2002**, *65*, 165401.
- (28) Dion, M.; Rydberg, H.; Schröder, E.; Langreth, D. C.; Lundqvist, B. I. Van der Waals Density Functional for General Geometries. *Physical Review Letters* **2004**, *92*, 246401.
- (29) Klimeš, J.; Bowler, D. R.; Michaelides, A. Chemical accuracy for the van der Waals density functional. *Journal of Physics: Condensed Matter* **2010**, *22*, 022201.
- (30) Troullier, N.; Martins, J. L. Efficient pseudopotentials for plane-wave calculations. *Physical review B* **1991**, *43*, 1993.
- (31) Frederiksen, T.; Paulsson, M.; Brandbyge, M.; Jauho, A.-P. Inelastic transport theory from first principles: Methodology and application to nanoscale devices. *Physical Review B* **2007**, *75*, 205413.
- (32) Transport code and tools based on SIESTA and TranSIESTA URL <http://sourceforge.net/projects/inelastica/>.
- (33) Rozzi, C. A.; Varsano, D.; Marini, A.; Gross, E. K. U.; Rubio, A. Exact Coulomb cutoff technique for supercell calculations. *Physical Review B* **2006**, *73*, 205119.

Quantum Dots embedded in Graphene Nanoribbons by Chemical Substitution: Supporting Information

Eduard Carbonell-Sanromà,[†] Pedro Brandimarte,^{‡,¶} Richard Balog,^{†,§,||} Martina Corso,^{†,‡,§} Shigeki Kawai,^{⊥,#,@} Aran Garcia-Lekue,^{¶,§} Shohei Saito,^{@,△} Shigehiro Yamaguchi,[▽] Ernst Meyer,[#] Daniel Sánchez-Portal,^{‡,¶} and Jose Ignacio Pascual^{*,†,§}

[†]*CIC nanoGUNE, Tolosa Hiribidea 76, 20018 Donostia-San Sebastian, Spain*

[‡]*Centro de Fisica de Materiales, 20018 Donostia-San Sebastian, Spain*

[¶]*Donostia International Physics Center, 20018 Donostia-San Sebastian, Spain*

[§]*Ikerbasque, Basque Foundation for Science, Bilbao, Spain*

^{||}*Department of Physics and Astronomy, Aarhus University, 8000 Aarhus C, Denmark*

[⊥]*99 International Center for Materials Nanoarchitectonics, National Institute for Materials Science, 1-1, Namiki, Tsukuba, Ibaraki 305-0044, Japan*

[#]*Department of Physics, University of Basel, CH-4056 Basel, Switzerland*

[@]*PRESTO, Japan Science and Technology Agency, Kawaguchi, Saitama 332-0012, Japan*

[△]*999 Department of Chemistry, Graduate School of Science, Kyoto University, Kitashirakawa Oiwake, Sakyo, Kyoto 606-8502, Japan*

[▽]*Institute of Transformative Bio-molecules, Nagoya University, Furo, Chikusa, Nagoya 464-8602, Japan*

E-mail: ji.pascual@nanogune.eu

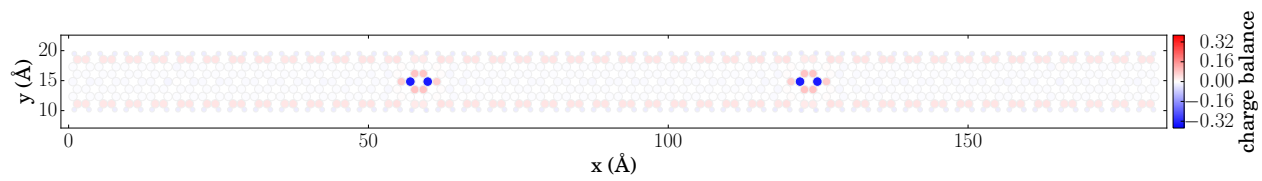


Figure S1: Mulliken population analysis of the freestanding hybrid 2B-7-AGNR. The boron atoms are negatively charged, receiving an amount of ~ 0.38 electron charge from the neighbouring carbons which, in turn, are positively charged.

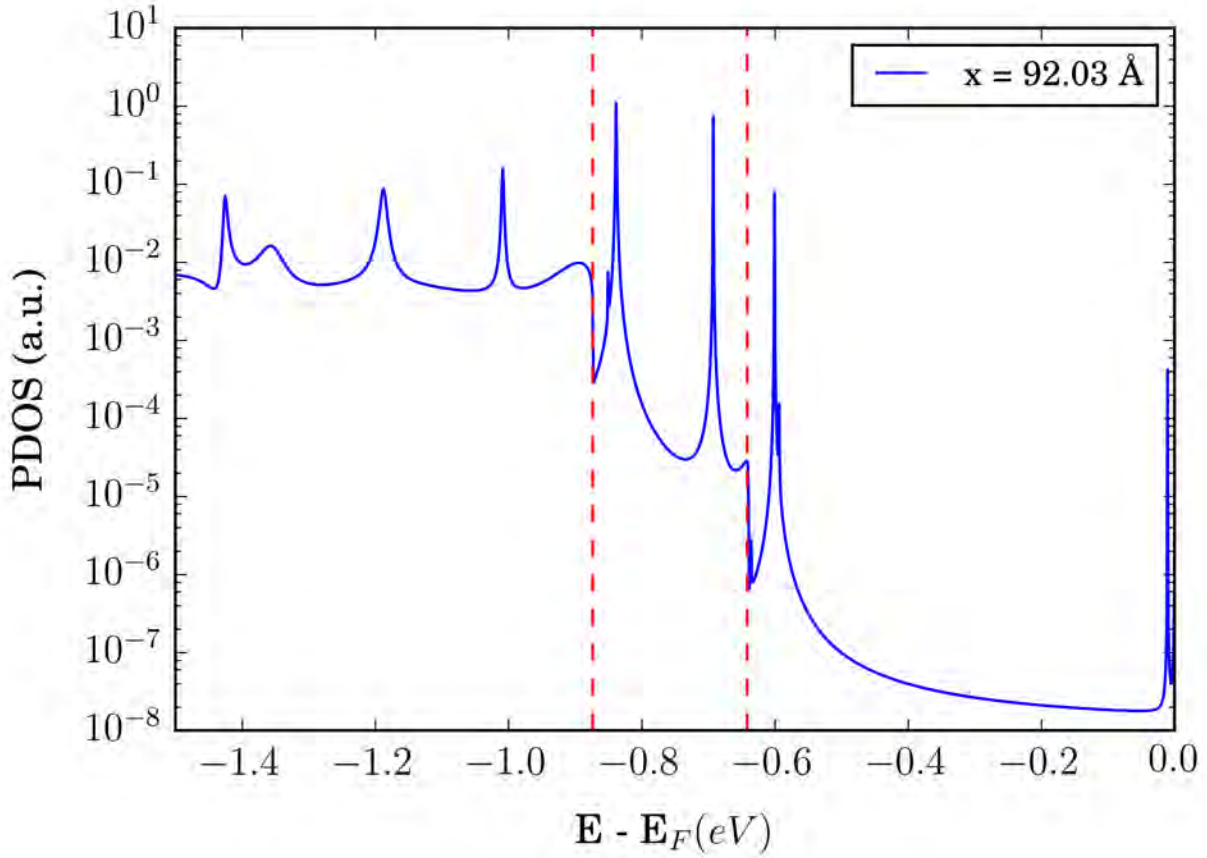


Figure S2: Projected DOS from a pristine segment enclosed between two borylated sections 6.5 nm apart. The plot is obtained at the middle position between the two borylated sections. The vertical dashed red lines correspond to onsets of the pristine VB ($\sim -0.64 \text{ eV}$) and VB-1 ($\sim -0.87 \text{ eV}$). With the log-scaled PDOS the increase of intensity coming from the VB-1 is clearly seen.

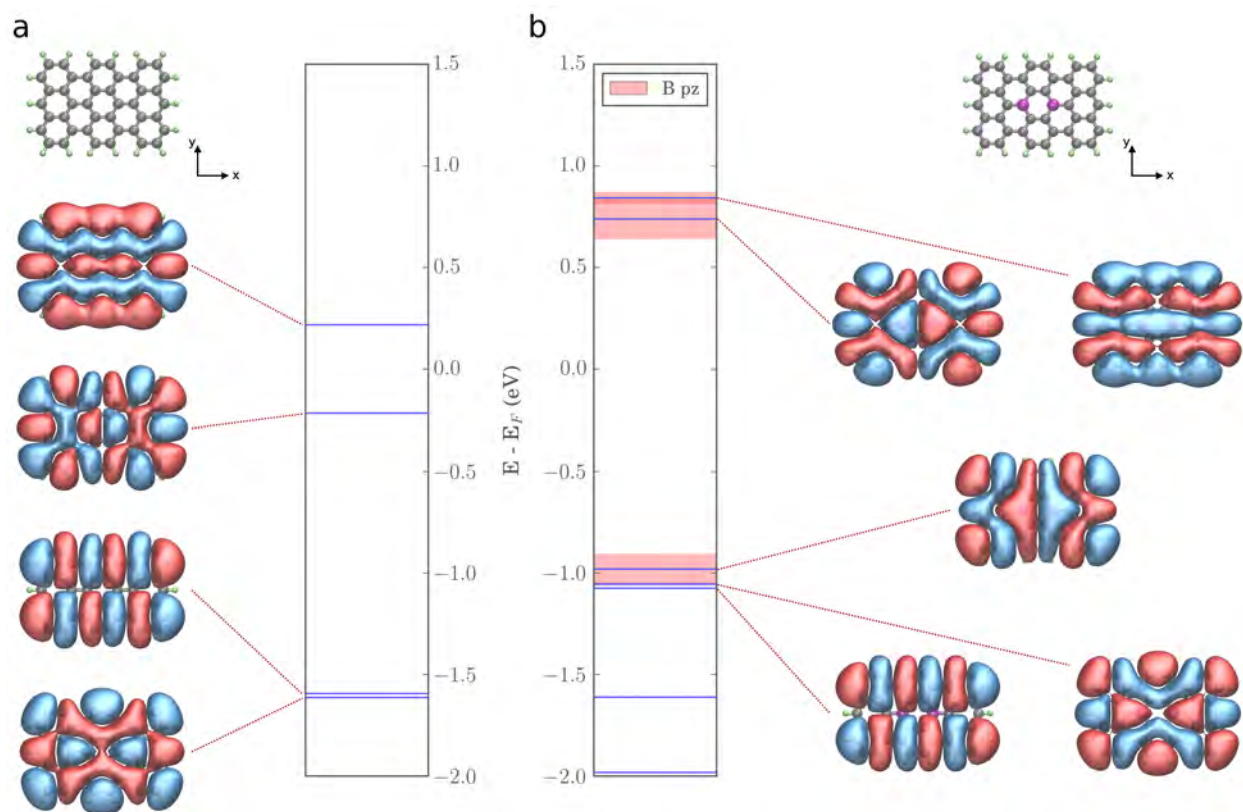


Figure S3: Wave functions and corresponding energy levels obtained for a pristine trisanthene molecule (a) and for a trisanthene molecule with a substituted pair of boron atoms (b). In the considered energy range, the boron-substituted molecule presents a new energy level (at $E - E_F = -0.98$ eV) with strong boron p_z character. The wave function of the boron induced level shows an even symmetry with respect to the mirror plane bisecting the molecule along x direction and an odd symmetry regarding the plane bisecting along y .

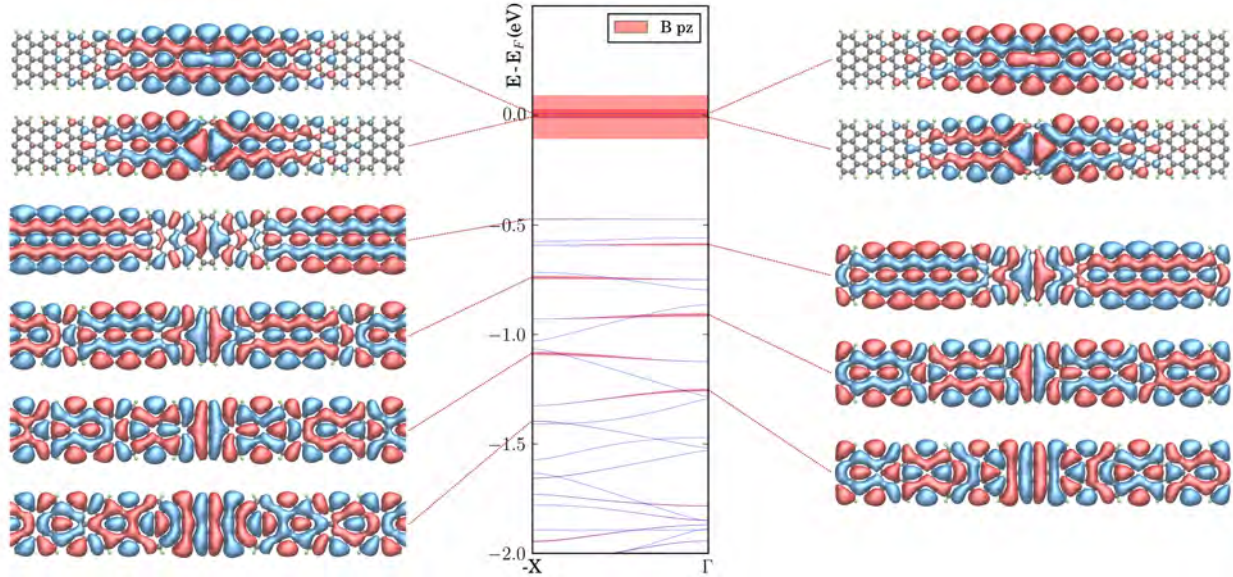


Figure S4: Band structure (center) obtained for a 7-AGNR with a periodic boron pair substitution. The unit cell of the ribbon has been chosen so that the distance between the boron dimer and its next periodic replica is equal to that of the open system calculation, namely 65 Å. Two defect levels, localized around the boron pair, are identified close to the Fermi energy. The band corresponding to the pristine nanoribbon valence band (VB) strongly hybridizes with a boron resonance and appears with a stronger boron p_z character alternately at Γ and $-X$ points. This uneven k-point distribution is related to the nodal structure imposed by the relevant boron resonance shown in Fig S3. Due to this hybridization between the boron and carbon states, the VB is split into a collection of almost flat subbands and presents bigger gaps at the boundary of the Brillouin zone when compared to the VB-1. The corresponding wave functions are shown on the left for $-X$ and on the right for Γ . One observes a nodal structure analogous to that of the eigenchannel wave functions calculated at the resonance energies. Starting with $n=1$ at $-X$ ($E - E_F = -0.47$ eV), $n=2$ at Γ ($E - E_F = -0.59$ eV), and so forth, all these wave functions show an even symmetry with respect to the mirror plane bisecting the nanoribbon along its axis. Moreover, one notices that a phase change of π is imposed at the plane between the boron atoms, similarly to the boron induced state obtained in the isolated molecule calculation.

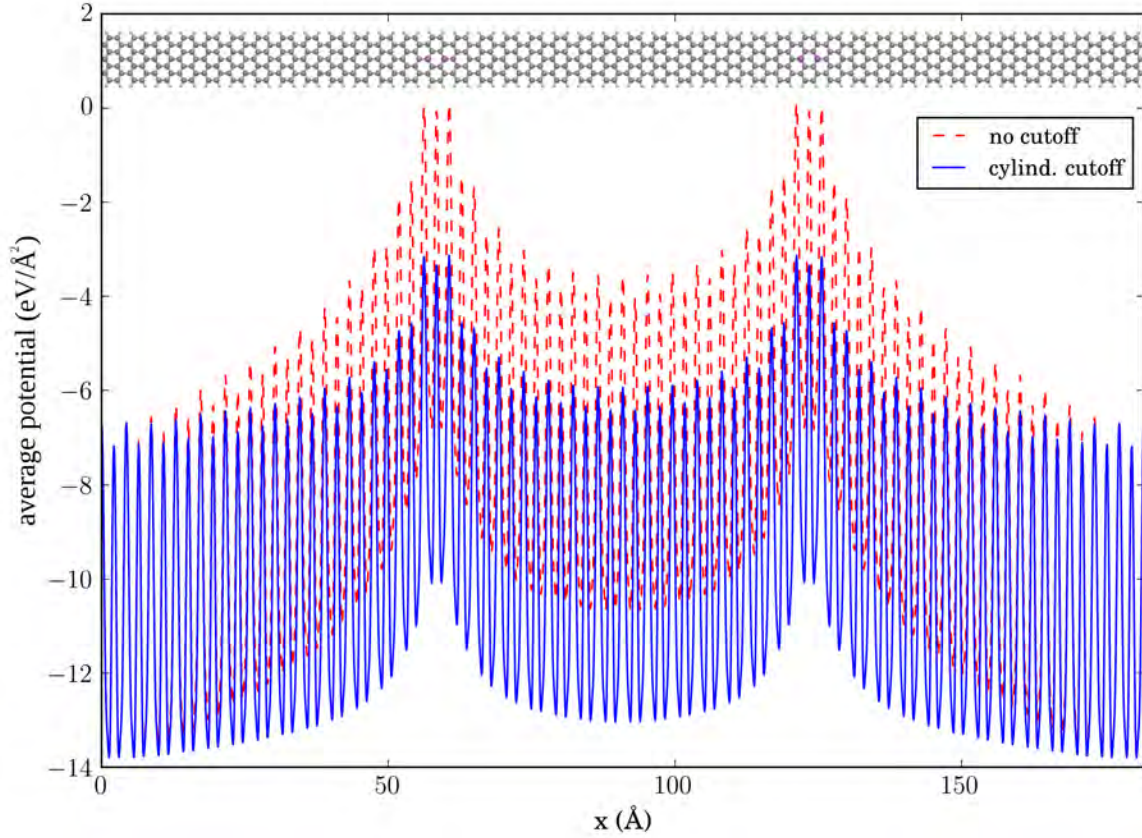


Figure S5: Laterally averaged electrostatic potential (Hartree potential plus local pseudopotential) obtained for the open system calculation of the hybrid 2B-7-AGNR, before (red) and after (blue) applying a cylindrical cutoff for the Coulomb interaction, with 12.5 Å cutoff radius. The small dipole created between the inner “quantum-well” and the outer “electrode” regions interacts via the long range part of the Coulomb potential with the periodic replicas along the directions perpendicular to the nanoribbon axis, even after considering a large vacuum region between them (we used a unit cell with 30 Å along both perpendicular directions). This artifact is removed after applying the cutoff, rendering the system really one-dimensional in spite of the periodic boundary conditions used in the calculations. The slow decay of the electrostatic potential around the boron defects is a signature of their small charging. Mulliken population analysis indicates that $0.37e$ charge is donated to each boron atom by the surrounding carbons (Figure S1). The remaining electrostatic background causes a small upward shift of the bands in the pristine confined segment of the hybrid 7-AGNR. As a result, the $n=1$ mode in Fig. 4a appears at -0.6 eV, a value higher than the onset of the pristine 7-AGNR bands and transmission step in Fig. 4b, at -0.64 eV. Since the $n=1$ mode lies above the bands injecting electrons in the 7-AGNR contacts, it cannot contribute to the transmission, and the first transmitting mode is the $n=2$, as seen in Fig. 4d. This effect is due to considering free-standing hybrid 7-AGNRs. In the experimental situation, the additional screening provided by the metal substrate is expected to eliminate this electrostatic background.

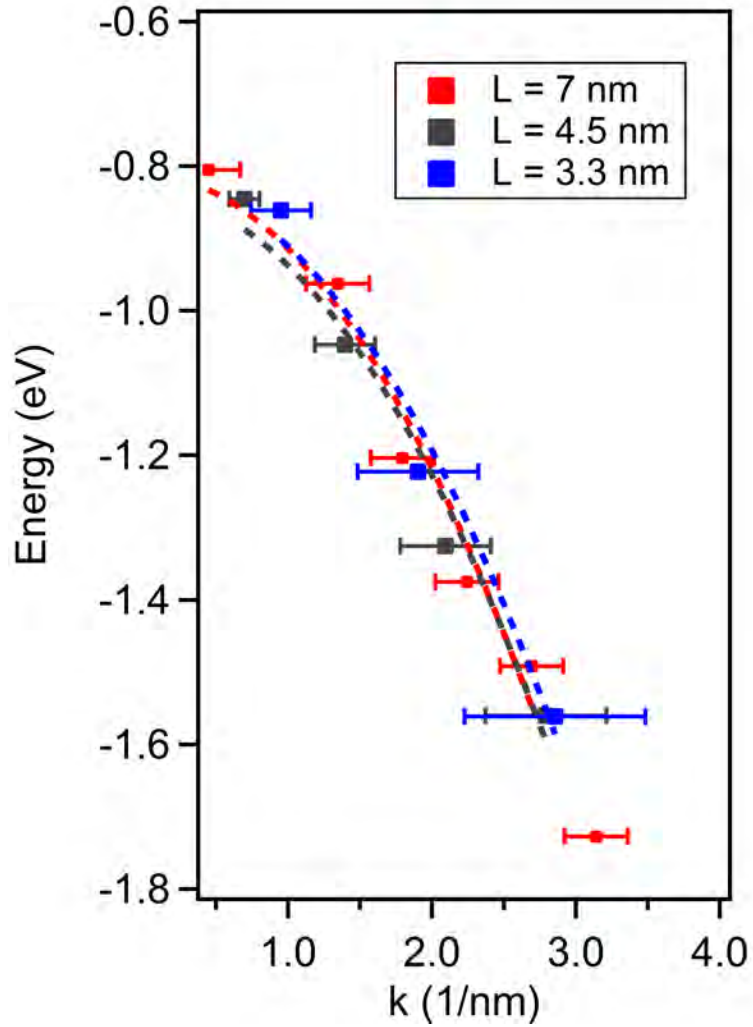


Figure S6: Energy dispersion relation ($k = n\pi/L$) for three quantum wells of different lengths. The data in red corresponds to the QW shown in Figure 3b of the manuscript for comparison. Dashed lines show parabolic fits to each data set, showing a good overlay of all energy dispersions.